Journal of Materials Chemistry A

PAPER

Cite this: J. Mater. Chem. A, 2019, 7, 19996

A water-resilient carbon nanotube based strain sensor for monitoring structural integrity†

Preety Ahuja,[a] Shingo Akiyama,[a] Sanjeev Kumar Ujjain,[a] Radovan Kukobat,[a] Fernando Vallejos-Burgos,[a] Ryusuke Futamura,[a] Takuya Hayashi,[b] Mutsumi Kimura,[c] David Tomanek[d] and Katsumi Kaneko *[a]

Received 25th June 2019
Accepted 6th August 2019

DOI: 10.1039/c9ta06810d

rsc.li/materials-a

Monitoring structural integrity during and after extreme events such as an earthquake or a tsunami is a mundane yet important task that still awaits a workable solution. Additionally, the mechanical frame strength of transportation must be continuously monitored for sufficient safety. Currently available sensors are not sufficiently robust and are affected by humidity. A water-proof strain sensor would be applicable for infrastructure safety management in harsh environments and also as an advanced wearable sensor. Here, we develop a strain sensor based on single-walled carbon nanotubes (SWCNTs) encapsulated in a non-fluorinated superhydrophobic coating, providing water resistance during elastic deformation, even at 100% strain. This newly developed sensor also offers highly linear piezoresistive behaviour owing to stretchable SWCNT networks. The superior water resiliency of the sensor, along with its appealing linearity and high stretchability, demonstrates the scalability of this approach for fabricating efficient strain sensors for applications in infrastructure and robotic safety management.

1. Introduction

Governments must guarantee safe environments to preserve life while maintaining a comfortable urban landscape with minimal economic burden. In particular, numerous infrastructures, such as buildings, bridges and tunnels, in advanced countries have serious deterioration issues. Additionally, the mechanical frame strength of transportation means, such as cars, aircraft, ships, and trains, must be continuously monitored for safety. Consequently, an internet-mediated sensing system needs to be established to support appropriate renovations; such a system would require the use of strain sensors that are highly stable even in harsh environments. The development of high-sensitivity water-proof strain sensors is urgently needed; in particular, non-fluorinated water-proof sensors are preferable for assuring safety. Currently, there are no active studies on sensors for monitoring structural integrity, although there have been many reports on wearable sensors.[1,2] Some of these sensors can be efficiently applied for monitoring structural integrity with enhanced environmental tolerance.[3] However, the sensing ability of existing sensors is limited in terms of underwater detection, and only a few reports have suggested sensors with underwater sensing capability.[4–7] The approaches for producing water resistive sensors are still associated with limitations involving hysteresis and lower strain tolerance. However, chemically safe superhydrophobic smart coatings for stretchable sensors with sustained piezoresistive responses have yet to be realized.

Carbon nanotubes represent the foundation for most of the conventional stretchable strain sensors,[1,8–13] owing to performance characteristics which considerably exceed those of known metal/metal oxide or organic semiconductor based sensors.[14–16] More precisely, single-walled carbon nanotubes (SWCNTs) offer high internal piezoresistivity for use in strain sensors.[17,18] The main challenge in their use as a sensing element follows from the restrictions associated with the device fabrication strategies and lack of integration of individual elements into stretchable systems.[19–25] Previously, fragmented SWCNT paper with cracks was integrated into PDMS, which endowed the device with a large gauge factor under 50% strain.[26] A thickness gradient SWCNT film exhibited segmented sensitivity with substantial structural changes under applied strain, thereby providing a non-linear response.[27] Despite this progress, an enhanced initial resistance and a non-linear response (sensitivity deviation) are always associated, increasing the need for complicated calibration.[28] This may be attributed to the release of strain energy *via* fracture of CNT junctions[29–32] due to unfavourable contact between SWCNTs owing to their insufficient dispersion in PDMS. A newly

[a]Research Initiative for Supra-Materials, Shinshu University, Nagano, Japan. E-mail: kkaneko@shinshu-u.ac.jp

[b]Department of Water Environment and Civil Engineering, Faculty of Engineering, Shinshu University, Nagano, Japan

[c]Faculty of Textile Science and Technology, Shinshu University, Ueda, Japan

[d]Physics and Astronomy Department, Michigan State University, East Lansing, Michigan 48824, USA

† Electronic supplementary information (ESI) available. See DOI: 10.1039/c9ta06810d

developed Zn–Al sol gel dispersant for SWCNT bundles developed by our group is promising to stably embed the SWCNT network in PDMS.[33]

Taking advantage of stable SWCNT networks in PDMS, we report a superhydrophobic strain sensor with excellent linear response and marked water resiliency under elastic deformation. Good electrical contact between SWCNTs is guaranteed by molecular level anchoring of SWCNTs in PDMS, resulting from weak charge transfer interactions as demonstrated by *in situ* Raman spectroscopy. In addition, this sensor is capable of detecting very less strain of 0.1% even without any amplification device, endowing a potential sensor for monitoring structural integrity under harsh conditions.

2. Results and discussion

2.1 Water-proof strain sensor

Firstly, SWCNTs were dispersed in water with the Zn–Al sol–gel dispersant following a previously described protocol.[33] The creased SWCNT film resulting from the film transfer approach was further utilized for making a water resistive PDMS embedded strain sensor (PDMS/SWCNT/PDMS) as shown in Fig. S1.†

The newly developed sensor (Fig. 1a) exhibits a contact angle of $161.5^\circ \pm 0.8$ and this superhydrophobicity is remarkably maintained even when the sensor is stretched with 100% strain as shown in Fig. 1b, supported with SEM micrographs (Fig. S2†). SEM micrographs of the superhydrophobic surface of the sensor show dual scale morphology, where nanoscale pseudo-spherical particles of SiO_2 aggregate to form microscale clusters. These clusters having dual scale roughness are covered with a layer of PDMS, which not only decreases their surface energy but also maintains their structural integrity, and hence provides stable superhydrophobicity even in the strained state. The effectiveness of the superhydrophobic coating is evidenced by the smaller contact angle ($108^\circ \pm 2$) of the sensor without the water-repellent coating. This is further demonstrated in Video V1 by its ability to block the water jet falling on the sensor in both the relaxed and stretched states (Fig. S2†). No water residue remained on the surface of the water-proof sensor after testing under the water jet in contrast to the bare sensor (without water-repellent coating), which demonstrates the robustness of the water-repellent coating of the sensor. Notably, the water-repellence was maintained in corrosive environments, such as in acidic, alkaline or saline aqueous solutions (Video V1) evidencing their applicability in harsh environments. We also traced the stability of the superhydrophobic coating on the sensor by storing the sensor in water for 100 h.

We found that the contact angle did not change even after 100 h, suggesting the reliable applicability of the sensor under water (Fig. 1c). In addition, the piezoresistive response of the water-repellent sensor was observed under humid conditions by packing the sensor between wet sponges (Fig. 1d) and subjecting it to consecutive loading-unloading cycles to 100% strain. The arrangement of the sensor between dry and wet sponges is shown in Fig. S3.† The response to the applied strain showed no piezoresistive change (within reproducibility) under dry and wet conditions (Fig. 1e), demonstrating the successful deposition of the superhydrophobic coating on the fabricated sensor. The actual response of the sensor with and without the superhydrophobic coating under humid conditions is shown in Fig. S3.† Such a performance has not been observed previously in CNT based stretchable strain sensors.

2.2 Comparative piezoresistive performance

Besides superhydrophobicity, the realization of a highly linear piezoresistive response may now be possible. Previously, others reported highly stretchable CNT based strain sensors but they are associated with large sensitivity deviations. For further understanding, a comparison with the piezoresistive performance of fabricated sensors published in the literature on SWCNT based strain sensors is shown in Fig. 1f–g. Here, the plots begin above 3% strain due to the lack of data in the literature and are drawn to scale to show the actual response behaviour. The sensor reported by Z. Liu *et al.*[27] gives a linear response at a lower strain with a high relative resistance change as shown in Fig. 1f. However, the linear plot deviates in the large strain range. The response curve by Park *et al.*[28] shows an extremely low relative resistance change. The remaining one by Zhou *et al.*[26] shows a high relative resistance change along with a strain tolerance of 50% with a non-linear response. A reliable and linear response is the key to reproducibility of the stretchable strain sensor. Our sensor exhibits a complete linear response passing through the origin with a consistent sensitivity, even below 1% strain. Also, we need to discuss the performance of the sensor with regard to sensitivity (gauge factor). Our PDMS/SWCNT/PDMS sensor shows almost no change in the gauge factor over the whole stretchability range (Fig. 1g), demonstrating the linear response of the sensor. However, the gauge factor reported in the literature[26,27] showed a large deviation with the strain. The gauge factor in the literature[28] is almost constant but the absolute value is too small. Consequently, the present PDMS/SWCNT/PDMS sensor has excellent performance in comparison with the previously reported sensors.

2.3 Concerted interaction between SWCNTs and PDMS under strain

The effect of structural deformation on the fabricated sensor was evaluated by observation with *in situ* optical microscopy, before (Fig. 2a–c) and after cycling (Fig. 2d–f). The concerted motion of the SWCNTs with PDMS in response to applied strain demonstrates the opening of the creases at lower strains, along with crack formation and propagation at higher strains. It is clearly shown that the well dispersed SWCNTs on PDMS enabled stretchable connection throughout the cracks, leading to good electrical contact, even at higher strains. In addition, these cracks vary linearly with the applied strain (Fig. 2g) while maintaining stable electrical contact during strain loading-unloading cycles, causing a linear sensor response. The first loading-unloading cycle stabilizes the inter SWCNT contacts in PDMS, thereby inducing constricted cracks (Fig. S4a–e†) giving an initial irreversible response (Fig. 2g). The second loading-

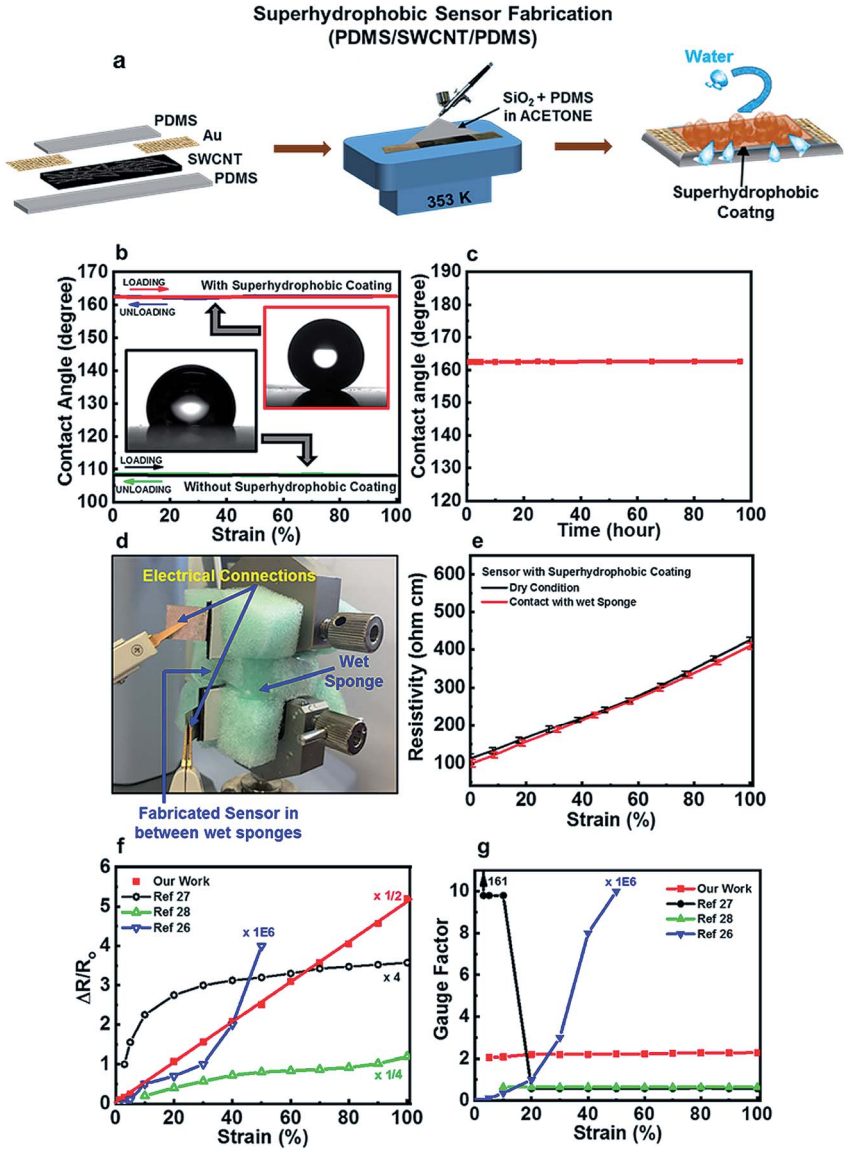

Fig. 1 (a) Schematic of the device structure. (b) Contact angle variation at different applied strains. The insets show images of the contact angle at particular strains. (c) Time course evaluation of the contact angle on the water-repellent sensor. (d) Image of the sensor between wet sponges. (e) Resistivity change of the water-repellent sensor in response to applied strain when in contact with dry and wet sponges. Error bars represent standard error. Comparative performance of the fabricated sensor in terms of (f) Relative resistance change in response to applied strain and (g) gauge factor with the existing literature on SWCNT based stretchable strain sensors.

unloading cycle produces no new cracks (Fig. S4f–j†), leading to a reversible and reproducible linear response.

The stretching decreases the electrical contact area between the well-connected SWCNTs resulting in gentle resistance increments without discontinuation of the electrically conducting networks at higher strains, thus allowing a highly linear piezoresistive response over a wide stretching range. Furthermore, the effect of continuous stretching and releasing for several cycles was observed in optical images (Fig. 2d–f) recorded at different strains. A more stabilized network of SWCNTs is formed, in which some of the SWCNTs interact more strongly with each other and undergo structural variations, resulting in more agglomerated stacks.

Notably, the wide and short cracks (Fig. 2c) formed during the initial loading-unloading process at 100% strain become steadier with narrower counterparts (Fig. 2f) due to weaker PDMS intercalation. Consequently, a more stabilized response is attained after continuous loading-unloading cycles. The parallel contact with great stability must be guaranteed by molecular level contact between SWCNTs and PDMS. We recorded *in situ* Raman spectra in accordance with the optical images for two areas, *i.e.*, black and white areas resulting from crack propagation. The black and white areas stem from different SWCNT density distributions in response to the applied strain. At higher strains, well connected SWCNTs have a smaller contact area with reduced density in particular

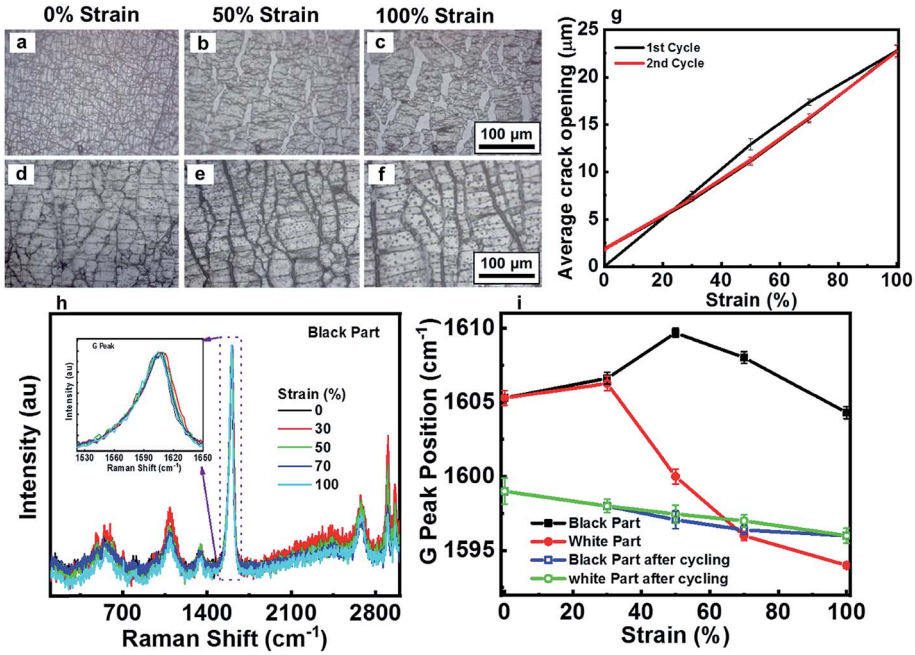

Fig. 2 *In situ* optical micrographs of the sensor under different strains, before (a–c) and after (d–f) cycling. (g) Average crack opening during initial cycles at particular strains. Error bars denote standard error. (h) Raman spectra showing variations in the G-band peak position at different strains for the black part. (i) Quantitative shift of the G-band peak position with applied strain for the black and white part, before and after cycling. Error bars represent standard error.

regions, imparting more transparency (white area) due to PDMS intercalation. This presence of SWCNTs in the white area is excitingly evidenced by the existence of G-band peaks at higher strains in the Raman spectra (Fig. S5†). The G-band peak of the SWCNTs in the black area is observed at 1604 cm^{-1} (Fig. 2h) due to the in-plane vibration of carbon–carbon bonds, whereas the G-band peak of bare SWCNTs is at 1589 cm^{-1}. This blue shift *versus* the pristine SWCNTs is attributed to the charge transfer from the SWCNTs to PDMS.[33–36]

The G-band peak shift for the black and white areas *versus* strain is shown in Fig. 2i. The black and white areas exhibit the same G-band peak position at the initial stage up to 30% strain. The effect of the charge transfer interaction between the SWCNTs and PDMS on strain causes the shift in the G-band peak position. The black area shows an upshift to 50% strain followed by a downshift at higher strains, while the white area displays downshifting beyond 30% strain. This behaviour is different from the literature results indicating strain causes a simple downshift in the G-band peak position.[37–39] Our experiment clearly shows that the black and white areas play different roles. We must take into account two factors regarding the different shift behaviours of the G-band peak position with strain. One is the charge transfer interaction of the SWCNTs with the PDMS surface due to the disentanglement of SWCNTs in the film. The other is the isolation of the SWCNTs from PDMS with weaker charge transfer interactions. In the black area at lower strains, well dispersed and entangled SWCNTs undergo disentanglement[33] by dissipating strain through creases and thus interact more strongly with PDMS. However, the latter factor is dominant at higher strains, inducing weaker charge transfer interactions between the isolated SWCNTs and PDMS. This change consequently weakens the interaction among nearby SWCNTs and lowers their vibrational frequency.[40] A similar G-band peak shift is observed at lower strains up to 30% for the white area; the lower SWCNT content and weaker contact of the SWCNTs with PDMS induce a greater downshift in the G band. The G band for the black and white areas shows a similar slight downshifting in response to the applied strain after several repeated loading-unloading cycles. This gradual shift of the G-band peak position of SWCNTs indicates the stably connected SWCNT contacts and the corresponding less charge transfer interaction with PDMS. Therefore, we can obtain a good linear piezoresistive response to strain.

2.4 Linear response of electrical resistance against strain

The linear *I–V* characteristics of the sensor (PDMS/SWCNT/PDMS) demonstrate ohmic contact (Fig. S6†), enabling the use of the assembled configuration as a strain sensor (Fig. S7†). The sensor was then subjected to 100% strain using a stretching machine at a rate of 1 mm s^{-1} and the corresponding change in resistance was recorded. Fig. 3a shows the state of the sensor when strained (100%) and unstrained (0%). The resistance change with strain during loading and unloading follows monotonic and linear increments following the strain path (Fig. 3b). This one-to-one correspondence in resistance output with the applied strain makes the device suitable for effectively detecting strain[41] during infrastructure monitoring. The behaviour of the initial loading-unloading cycle is different from that of subsequent cycles owing to the irreversible resistivity loss during the first cycle, which was attributed to the

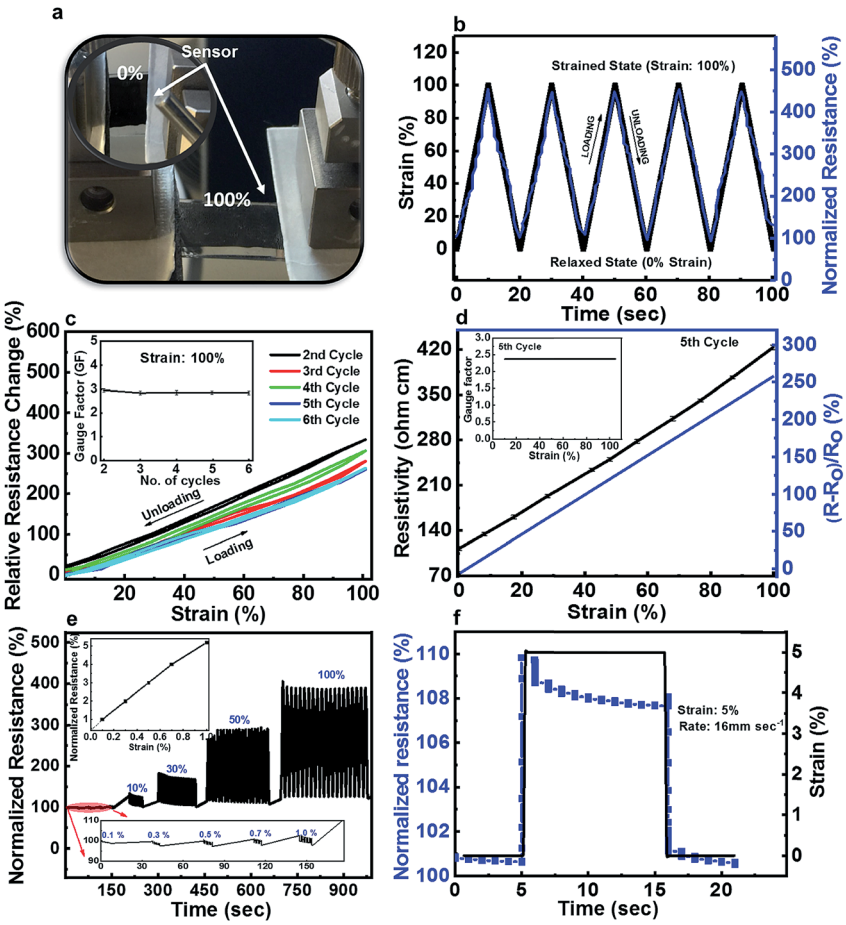

Fig. 3 (a) Image of the sensor at 0% and 100% strain. (b) Relative resistance change and strain variation with time during initial cycling of the sensor. (c) Resistivity change with strain for six consecutive initial cycles. (d) Resistivity and relative resistance change of the sensor with strain (5th cycle) showing a highly linear response. (e) Normalized resistance change with increasing strain. (f) Response time of the sensor during quasi-transient loading (5% strain at 16 mm s^{-1}).

remaining narrower cracks during the unloading of the first strain cycle as observed earlier. The results of further cycles are shown in Fig. 3c, demonstrating a stabilized relative resistance change with strain in the initial five strain loading-unloading cycles with a very small degree of hysteresis, ~2% in the last few cycles. The relative resistance change with strain represents the sensitivity of the sensor in terms of the gauge factor (GF).[42] The sensitivity (GF) of the sensor at 100% strain was found to be constant, as shown in the inset of Fig. 3c during the initial cycles. The linear resistance change with strain was also observed across the whole stretchability range of 100% (R^2 0.97), even after five cycles of stabilization (Fig. 3d). Thus, the fabricated sensor possesses high sensitivity (GF ~2.4), not only at 100% strain but also at lower strains (Fig. 3d inset), compared to the earlier reported values.[7,43,44] The sensitivity of the sensor at every strain is similar (inset, Fig. 3d), evidencing the linear response of the fabricated sensor. The linear strain-induced resistance change through the change in the SWCNT–SWCNT contact area with the strain, is promising for infrastructure monitoring.

An additional advantage of the present sensor is its high sensitivity to detect lower strains with a fast response. This sensor can detect as little as 0.1% strain and as much as 100% strain with a highly linear and stable response (Fig. 3e), even using only the linear relationship between resistance and lower strain (Fig. 3e inset). The application of field effect transistors to this strain sensor should easily enable the detection of strains less than 0.01%. Furthermore, the response and recovery time are measured by loading the sensor with a quasi-transient step (5% strain at 16 mm s^{-1}) and holding the strain for a particular time to determine the drift.[45] The corresponding resistance change during loading and unloading strain occurred within less than 100 ms (Fig. 3f), demonstrating the ultrafast response and recovery properties facilitating the detection of strain at a very low angle for structural monitoring. In addition, only ~2% drift in the resistance was observed during the initial stage of strain holding with no remarkable fluctuation, which is attributed to the viscoelasticity of PDMS;[46] this drift can be compensated using double sensors.

2.5 Structural transformation of the SWCNT network

The resistance variation mechanism of the present sensor originates from the stretchable SWCNT network with excellent electrical connections in PDMS. As the SWCNTs are highly dispersed on PDMS in the form of fine bundles of 40 nm size before straining,[47] the SWCNTs have a two-dimensionally developed random coil-like structure (Fig. 4a). The fine SWCNT coils begin to partially orient towards each other in PDMS when applying strain; the partially oriented SWCNT coils are in contact with the surrounding PDMS through the observed charge transfer interactions. The repeated strain application induces the formation of flocculated structures consisting of the fine SWCNT bundles, as shown by Transmission Electron Microscopy (Fig. 4b). The SWCNT coils grow into a stationary slip-flow state weakly supported by PDMS, as suggested by the smaller upshift of the Raman G-band peak, observed earlier. The SWCNT network corresponding to the flocculated structures of SWCNTs and PDMS, as confirmed by TEM observation (Fig. 4b1 and b2, before and after cycling, respectively) provides a linear response of the electrical resistance to the strain. This electrical contact is approximated by the following simple model, which neglects the capacitive factor.

The electrical conduction path of the SWCNT/PDMS sensor during a stationary response is governed by the flocculated structures consisting of SWCNT/PDMS blocks, block–block bridging contacts, and vacant regions, as shown in Fig. S8.† The total electrical resistance is simply described by the electrical resistance R between two arrays of SWCNT/PDMS blocks with inherent resistance R_I, as given by

$$R = \frac{2R_I R_B + 2R_I R_V + R_B R_V}{R_B + R_V} \quad (1)$$

Here, the gap resistance between the two arrays is expressed by the parallel resistance arrangement of the bridging contact resistance, R_B, and the resistance of the vacant region, R_V. The initial resistance reflects the inherent resistance, R_I, of the SWCNT/PDMS block. The formation of cracks in the film with strain increases the contribution of the parallel resistances of R_B and R_V. At lower strains, the whole resistance R is governed by only R_I as follows:

$$R = 2R_I \quad (2)$$

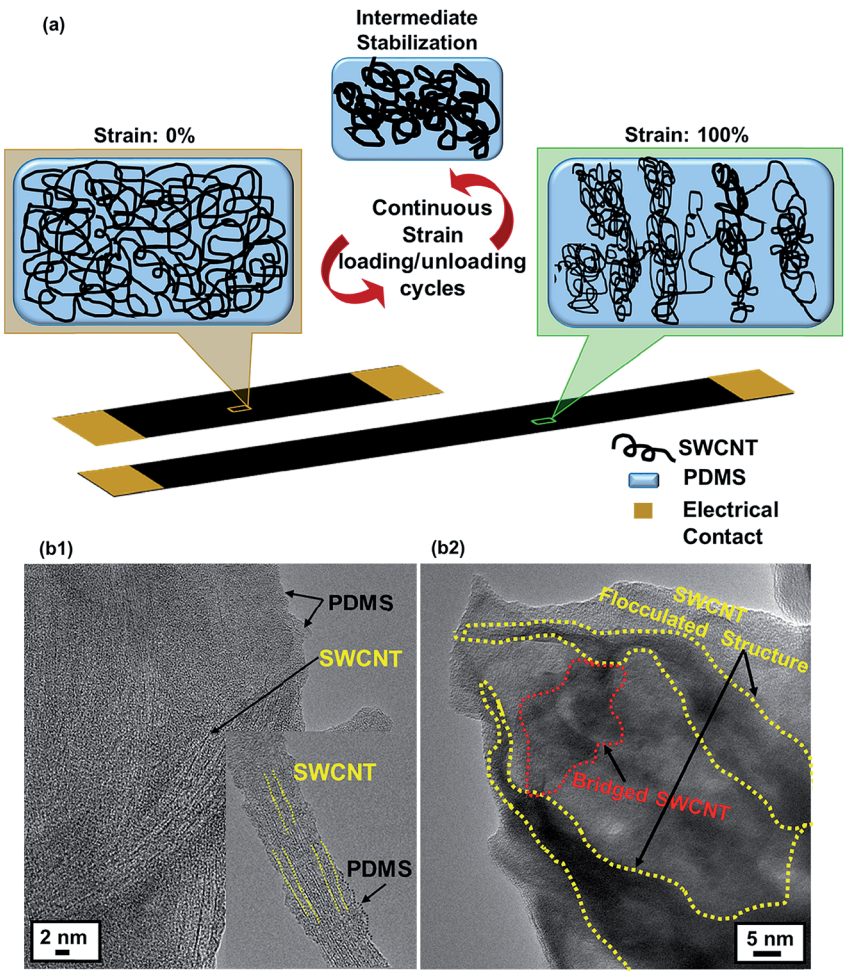

Fig. 4 (a) Model demonstrating stretching of the sensor to describe the deformation of the creases at lower strains and crack propagation at higher strains in agreement with TEM images (b1 and b2, before and after cycling, respectively).

This is because the contribution of R_V is negligible as there are insignificant vacant regions at lower strains.

Crack propagation is dominant at higher strains augmenting R_V. As $R_V \gg R_I$, R_B.

$$R = 2R_I + R_B \quad (3)$$

Here, R_B should be proportional to the decrease in the bridging contact with the increase in strain. The experimentally observed linear relationship between the resistance and strain, ε (Fig. S8†), leads to

$$R_B = 22.7 \times \varepsilon \text{ (ohm)} \quad (4)$$

Consequently, R_B and R at 100% stretching are calculated to be 2270 ohm and 5020 ohm, respectively, whereas experimentally observed R at 100% strain was 5125 ohm, supporting the above model.

2.6 Linear response performance after long-term cycling

The PDMS/SWCNT/PDMS sensor demonstrated stable performance, even after 15 000 cycles up to 100% strain, as shown in Fig. 5a. The precise resistance change is given in Fig. S9† and shows an increase in resistance due to the stabilization process during the initial cycles, followed by steady performance. This finding was further analysed by recording the resistance change with strain after certain cycles, as shown in Fig. 5b. After stabilization (7000 cycles), the sensor maintains a high linearity with augmented response with a Gauge factor ~5, especially at lower strains, highly reliable as compared to the previous sensors reported in infrastructure monitoring. Also, no further change was observed during its usage after stabilization, maintaining the highly linear response with negligible sensitivity deviations in a large strain spectrum up to 100%. These aforementioned characteristics impart distinguished performance to the fabricated sensor as compared to those in the literature (Table S1†).

The morphological changes during the loading-unloading cycles were analysed by SEM observation, before and after 15 000 cycles (Fig. S10†). New fine creases are generated after long-term cycling as evidenced from the 2D profile. The crease density in the PDMS/SWCNT/PDMS sensor increases from 400 ± 17 to 700 ± 12 mm^{-2} after these cycles. The increase in the crease density is key for producing a stable response, because the SWCNTs are connected with each other in the crease, providing stable conducting paths, as shown by SEM (inset, Fig. S11†).

2.7 Real-time responses

In order to determine the strength of the fabricated sensor, it is used for detecting strain in human finger motion and in a steel strip for real time applications in healthcare and infrastructure monitoring. We attached the prototype sensor to the forefinger of a glove *via* an adhesive (copper tape) and used it to characterize the motion of a human finger as an example of sensing real strain. Our sensor demonstrated a reproducible change in resistance in response to the strain applied by finger motion. The bending and relaxing of the finger were sensitively detected, as shown by the increase/decrease in the resistance (Fig. 6a, Video V1). In addition, a light-emitting diode (LED) can be modulated using this sensor, thus demonstrating its potential for application in intelligent visual control systems. We connected the LED with the fabricated sensor, and the illumination intensity varied in response to the strain applied to the senor (Fig. S12†)

Remarkably, the initial resistance of the sensor was low enough to light the LED using a 3 V battery (Video V1); the LED intensity sensitively depended on the strain applied. Further, we tested the structural integrity of steel and aluminum strips as they are inimitable engineering materials for infrastructure and industry. For this, the sensor was attached beneath the strips to sense the change caused by applying force by stretching the device (inset of Fig. 6b), and the sensor's resistance change in response to applied force (strain) on the strip was monitored. The fabricated sensor was able to monitor the strain in the aluminium and steel strips as shown in Fig. S12† and 6b. It can sense the change (even less than 1°) in the strips, revealing its potential efficacy in the regular inspection or structural monitoring of infrastructures.

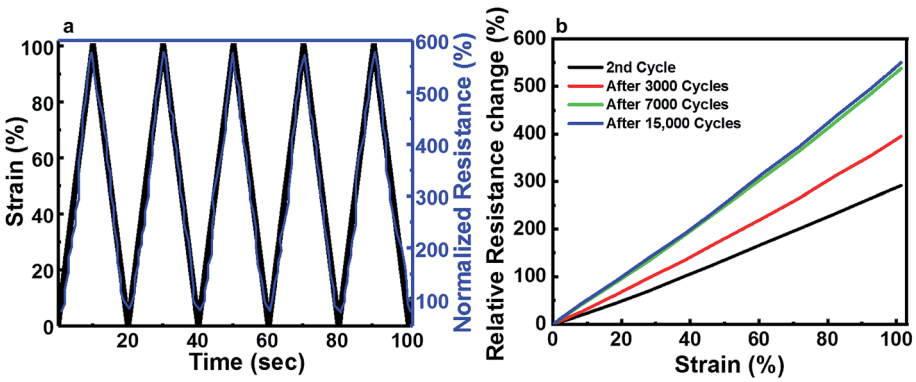

Fig. 5 (a) Normalized resistance change of the sensor after 15 000 cycles in response to an applied strain of 100%. (b) Relative resistance change with strain after particular cycles during cycling stability testing of the sensor.

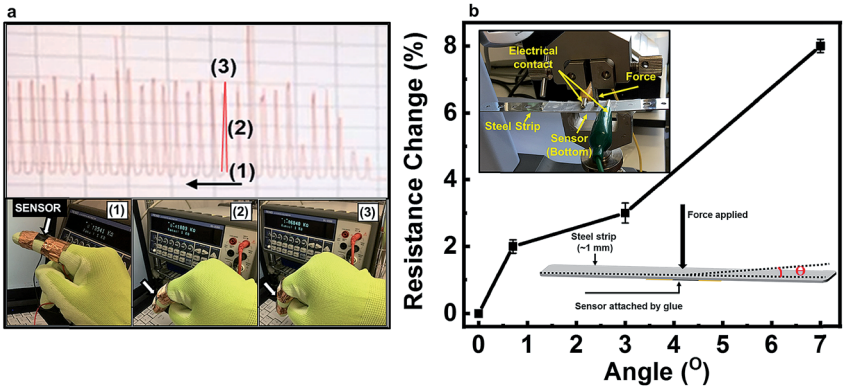

Fig. 6 (a) Real-time response of the sensor in detecting human finger motion. (b) Resistance change during strain detection (change in angle, degree) of a steel strip connected with the fabricated sensor.

3. Conclusions

We have successfully fabricated a superhydrophobic PDMS-embedded SWCNT strain sensor (PDMS/SWCNT/PDMS) from a well dispersed SWCNT film using a Zn–Al dispersant. This allows parallel contact between SWCNTs in response to an applied strain with a decrease in contact area leading to a linear increase in resistivity, capable of sustaining large strains (100%) with a highly linear response. This consequently prevented the failure of the electrically conducting network at higher strains, which has been associated with a non-linear or exponential piezoresistive sensor response, as mostly reported in the literature. The structural transformation of the SWCNTs into flocculated structures under continuous strain loading and unloading resulted in a more stabilized and augmented response especially at lower strains, evidencing their capability for efficient infrastructure monitoring. More importantly, the water resiliency of such a sensor will open many new pathways for a range of applications. We used non-fluorinated chemistry involving SiO_2 and PDMS to generate a low-energy surface, refraining from the utilization of environmentally hazardous materials to create a water-resilient coating on the sensor, even at 100% strain. This coating allows the sensor to function efficiently under humid, acidic, saline and alkaline conditions.

4. Experimental

4.1 Materials

Single walled carbon nanotubes (SWCNTs, dia. 2 nm) were purchased from Meijo Nano Carbon Co. Ltd. Zinc acetate, aluminium nitrate, ethanol, nitric acid, and silica were all purchased from Sigma Aldrich and used as received. PDMS and a curing agent were procured from Dow Corning Toray.

4.2 Fabrication of the SWCNT film

SWCNTs (dia. 2 nm; Meijo eDIPS) were homogeneously dispersed by the Zn–Al complex, as discussed in our previous report.[33] Briefly, 10 mg of SWCNTs was mixed with 100 mg of the Zn–Al complex in 20 mL of distilled water and ultrasonicated for 30 min using a homogenizer tip (SONIC VS 505). The solution was centrifuged (table top centrifuge, AS-185) at 7000 rpm for 45 min, and the supernatant was collected as SWCNT ink. A desired amount of SWCNT ink was spray-coated onto a glass slide (previously coated with 1% Zn–Al complex). The SWCNT-coated glass slide was dipped in 3 M HNO_3 (Sigma-Aldrich) for 2 min followed by washing in water, which resulted in a creased film due to removal of the Zn–Al dispersant from the surface. Interestingly, this film can be directly transferred onto any substrate and can form conformal contacts, making it favourable for integration into wearable electronics. In this study, we transferred the SWCNT film onto PDMS, as shown in Fig. S1a.†

4.3 Fabrication of the PDMS-embedded SWCNT strain sensor

The liquid PDMS (Dow Corning Toray) with a curing agent (10 : 1) was poured over homemade molds after degassing and cured at 75 °C to make a solid PDMS film. The creased SWCNT film was then transferred onto the PDMS film (4 × 1 cm^2), and electrical contact was made by sputtering gold onto the sides, leaving a 1 cm^2 area of the SWCNT film. Liquid PDMS with the curing agent (10 : 1) was poured over the assembly, leaving 0.5 cm of space from the sides for making contacts. The embedded structure was then cured at 75 °C for 2.5 h to obtain a SWCNT-based strain sensor with a thickness of 0.09–0.12 cm (Fig. S1b†). To produce the water-resilient coating, SiO_2 (Sigma-Aldrich, size: 5 nm) (50 mg) and PDMS with the curing agent (2 : 1) in acetone (10 mL) were dispersed by bath sonication for 5 min.[48,49] The resulting solution was spray-coated onto the sensor (1.5 mL on 3 × 1 cm^2) and cured at 80 °C for 0.5 h to make the sensor non-wettable (Fig. S1c†).

Acidic (10 mM HNO_3, pH 3), basic (10 mM NaOH, pH 10.8) and neutral (10 mM NaCl pH 6.8) solutions were also prepared to test the hydrophobicity of the sensor.

4.4 Characterization

The SWCNT film was characterized by using a SEM (SU 8000) and high resolution transmission electron microscope, HR-

TEM, JEM-2100F (JEOL). The surface morphology of the SWCNTs on PDMS was monitored *in situ* during a stretching/relaxing cycle *via* optical microscopy with *in situ* Raman spectroscopy (Jasco Laser Raman Spectrometer, NRS-4100). The mechanical properties and deformation of the SWCNT/PDMS sensor were measured with an automated instrument (EZ Test, EZ-SX, Shimadzu), and the data were recorded using a Trapezium X data logger. The electrical resistance of the sensor was measured using a digital multimeter (DL-2060, Texio) attached to the automated instrument.

Conflicts of interest

There are no conflicts to declare.

Acknowledgements

The work was supported mainly by the OPERA project from the JST and partially by a Grant-in-Aid for Scientific Research (B) (17H03039). RF and F V.-B. were supported by the Takagi Fund.

References

1 C. Liu, S. Han, H. Xu, J. Wu and C. Liu, *ACS Appl. Mater. Interfaces*, 2018, **10**, 31716–31724.
2 J. Wu, Z. Wu, X. Lu, S. Han, B.-R. Yang, X. Gui, K. Tao, J. Miao and C. Liu, *ACS Appl. Mater. Interfaces*, 2019, **11**, 99405–99414.
3 J. M. W. Brownjohn, *Philos. Trans. R. Soc., A*, 2007, **365**, 589–622.
4 J. Wu, Z. Li, X. Xie, K. Tao, C. Liu, K. A. Khor, J. Miao and L. K. Norford, *J. Mater. Chem. A*, 2018, **6**, 478–488.
5 R. Xu, K. Zhang, X. Xu, M. He, F. Lu and B. Su, *Adv. Sci.*, 2018, **5**, 1700655.
6 J. E. Mates, I. S. Bayer, J. M. Palumbo, P. J. Carroll and C. M. Megaridis, *Nat. Commun.*, 2015, **6**, 1–8.
7 L. Li, Y. Bai, L. Li, S. Wang and T. Zhang, *Adv. Mater.*, 2017, **29**, 1702517.
8 M. Amjadi, Y. J. Yoon and I. Park, *Nanotechnology*, 2015, **26**, 375501.
9 J. H. Kim, J.-Y. Hwang, H. R. Hwang, H. S. Kim, J. H. Lee, J.-W. Seo, U. S. Shin and S.-H. Lee, *Sci. Rep.*, 2018, **8**, 1–11.
10 J. Foroughi, G. M. Spinks, S. Aziz, A. Mirabedini, A. Jeirankhameneh, G. G. Wallace, M. E. Kozlov and R. H. Baughman, *ACS Nano*, 2016, **10**, 9129–9135.
11 S. Ryu, P. Lee, J. B. Chou, R. Xu, R. Zhao, A. J. Hart and S.-G. Kim, *ACS Nano*, 2015, **9**, 5929–5936.
12 Q. Li, K. Wang, Y. Gao, J. P. Tan, R. Y. Wu and F. Z. Xuan, *Appl. Phys. Lett.*, 2018, **112**, 1–4.
13 B. Hao, L. Mu, Q. Ma, S. Yang and P. Ma, *Compos. Sci. Technol.*, 2018, **163**, 162–170.
14 J. Lee, S. Kim, J. Lee, D. Yang, B. C. Park, S. Ryu and I. Park, *Nanoscale*, 2014, **6**, 11932–11939.
15 S. E. Root, S. Savagatrup, A. D. Printz, D. Rodriquez and D. J. Lipomi, *Chem. Rev.*, 2017, **117**, 6467–6499.
16 X. X. Gong, G. T. Fei, W. B. Fu, M. Fang, X. D. Gao, B. N. Zhong and L. D. Zhang, *Org. Electron.*, 2017, **47**, 51–56.
17 T. W. Tombler, C. Zhou, L. Alexseyev, J. Kong, H. Dai, L. Liu, C. S. Jayanthi, M. Tang and S.-Y. Wu, *Nature*, 2000, **405**, 769–772.
18 Alamusi, N. Hu, H. Fukunaga, S. Atobe, Y. Liu and J. Li, *Sensors*, 2011, **11**, 10691–10723.
19 D. Son, J. Lee, S. Qiao, R. Ghaffari, J. Kim, J. E. Lee, C. Song, S. J. Kim, D. J. Lee, S. W. Jun, S. Yang, M. Park, J. Shin, K. Do, M. Lee, K. Kang, C. S. Hwang, N. Lu, T. Hyeon and D. -H. Kim, *Nat. Nanotechnol.*, 2014, **9**, 397–404.
20 J. A. Rogers, T. Someya and Y. Huang, *Science*, 2010, **327**, 1603–1607.
21 L. Liu, Z. Niu, L. Zhang, W. Zhao, X. Chen and S. Xie, *Adv. Mater.*, 2014, **26**, 4855–4862.
22 M. Kollosche, H. Stoyanov, S. Laflamme and G. Kofod, *J. Mater. Chem.*, 2011, **21**, 8292.
23 D. J. Lipomi, M. Vosgueritchian, B. C.-K. Tee, S. L. Hellstorm, J. A. Lee, C. H. Fox and Z. Bao, *Nat. Nanotechnol.*, 2011, **6**, 788–792.
24 Z. Yang, D.-Y. Wang, Y. Pang, Y.-X. Li, Q. Wang, T.-Y. Zhang, J.-B. Wang, X. Liu, Y.-Y. Yang, J.-M. Jian, M.-Q. Jian, Y.-Y. Zhang, Y. Yang and T.-L. Ren, *ACS Appl. Mater. Interfaces*, 2018, **10**, 3948–3954.
25 T. Yamada, Y. Hayamizu, Y. Yamanoto, Y. Yomogida, A. I. Nazafabadi, D. N. Futuba and K. Hata, *Nat. Nanotechnol.*, 2011, **6**, 296–301.
26 J. Zhou, H. Yu, X. Xu, F. Han and G. Lubineau, *ACS Appl. Mater. Interfaces*, 2017, **9**, 4835–4842.
27 Z. Liu, D. Qiu, P. Guo, Y. Liu, B. Zhu, H. Yang, Y. Liu, B. Li, C. Zhang, J. Yu, B. Liedberg and X. Chen, *Adv. Mater.*, 2015, **27**, 6230–6237.
28 S. J. Park, J. Kim, M. Chu and M. Khine, *Adv. Mater. Technol.*, 2016, **1**, 1600053.
29 Y. Yu, S. Luo, L. Sun, Y. Wu, K. Jiang, Q. Li, J. Wang and S. Fan, *Nanoscale*, 2015, **7**, 10178–10185.
30 Q. Zhang, L. Liu, D. Zhao, Q. Duan, J. Ji, A. Jian, W. Zhang and S. Sang, *Nanomaterials*, 2017, **7**, 424.
31 B. Park, J. Kim, D. Kang, C. Jeong, K. S. Kim, J. U. Kim, P. J. Yoo and T. Kim, *Adv. Mater.*, 2016, **28**, 8130–8137.
32 D. Kang, P. V. Pikhitsa, Y. W. Choi, C. Lee, S. S. Shin, L. Piao, B. Park, K.-Y. Suh, T. Kim and M. Choi, *Nature*, 2014, **516**, 222–226.
33 R. Kukobat, D. Minami, T. Hayashi, Y. Hattori, T. Matsuda, M. Sunaga, B. Bharti, K. Asakura and K. Kaneko, *Carbon*, 2015, **94**, 518–523.
34 H.-Z. Geng, K. K. Kim, K. P. So, Y. S. Lee, Y. Chang and Y. H. Lee, *J. Am. Chem. Soc.*, 2007, **129**, 7758–7759.
35 A. M. Rao, P. C. Eklund, S. Bandow, A. Thess and R. E. Smalley, *Nature*, 1997, **388**, 257–259.
36 N. R. Raravikar, P. Keblinski, A. M. Rao, M. S. Dresselhaus, L. S. Schadler and P. M. Ajayan, *Phys. Rev. B: Condens. Matter Mater. Phys.*, 2002, **66**, 235424.
37 S. B. Cronin, A. K. Swan, M. S. Unlu, B. B. Goldberg, M. S. Dresselhaus and M. Tinkham, *Phys. Rev. Lett.*, 2004, **93**, 167401.
38 W. Yang, R. Z. Wang and H. Yan, *Phys. Rev. B: Condens. Matter Mater. Phys.*, 2008, **77**, 195440.

39 G. Wu, J. Zhou and J. Dong, *Phys. Rev. B: Condens. Matter Mater. Phys.*, 2005, **72**, 115411.
40 Z. H. Ni, T. Yu, Y. H. Lu, Y. Y. Wang, Y. P. Feng and Z. X. Shen, *ACS Nano*, 2008, **2**, 2301–2305.
41 X. Liao, Z. Zhang, Z. Kang, F. Gao, Q. Liao and Y. Zhang, *Mater. Horiz.*, 2017, **4**, 502–510.
42 X. Fan, N. Wang, J. Wang, B. Xu and F. Yan, *Mater. Chem. Front.*, 2018, **2**, 355–361.
43 J. Shi, X. Li, Y. Cheng, Z. Liu, L. Zhao, T. Yang, Z. Dai, Z. Cheng, E. Shi, L. Yang, Z. Zhang, A. Cao, H. Zhu and Y. Fang, *Adv. Funct. Mater.*, 2016, **26**, 2078–2084.
44 Y. Yu, Y. Luo, A. Guo, L. Yan, Y. Wu, K. Jiang, Q. Li, S. Fan and J. Wang, *Nanoscale*, 2017, **9**, 6716–6723.
45 Y. Cheng, R. Wang, J. Sun and L. A. Gao, *Adv. Mater.*, 2015, **27**, 7365–7371.
46 Y. Gao, X. Fang, J. Tan, T. Lu, L. Pan and F. Xuan, *Nanotechnology*, 2018, **29**, 235501.
47 R. Kukobat, T. Hayashi, T. Matsuda, M. Sunaga, T. Sakai, R. Futamura and K. Kaneko, *Chem. Phys. Lett.*, 2016, **650**, 113–118.
48 P. K. Roy, S. K. Ujjain, S. Dattatreya, S. Kumar, R. Pant and K. Khare, *Appl. Phys. A*, 2019, **125**, 535.
49 S. K. Ujjain, P. K. Roy, S. Kumar, S. Singha and K. Khare, *Sci. Rep.*, 2016, **6**, 35524.